

Sensitization of silicon by singlet exciton fission in tetracene

Markus Einzinger^{1,5}, Tony Wu^{1,5}, Julia F. Kompalla¹, Hannah L. Smith², Collin F. Perkins¹, Lea Nienhaus¹, Sarah Wieghold³, Daniel N. Congreve^{1,4}, Antoine Kahn², Moungi G. Bawendi¹ & Marc A. Baldo^{1*}

Silicon dominates contemporary solar cell technologies¹. But when absorbing photons, silicon (like other semiconductors) wastes energy in excess of its bandgap². Reducing these thermalization losses and enabling better sensitivity to light is possible by sensitizing the silicon solar cell using singlet exciton fission, in which two excited states with triplet spin character (triplet excitons) are generated from a photoexcited state of higher energy with singlet spin character (a singlet exciton)^{3–5}. Singlet exciton fission in the molecular semiconductor tetracene is known to generate triplet excitons that are energetically matched to the silicon bandgap^{6–8}. When the triplet excitons are transferred to silicon they create additional electron–hole pairs, promising to increase cell efficiencies from the single-junction limit of 29 per cent to as high as 35 per cent⁹. Here we reduce the thickness of the protective hafnium oxynitride layer at the surface of a silicon solar cell to just eight angstroms, using electric-field-effect passivation to enable the efficient energy transfer of the triplet excitons formed in the tetracene. The maximum combined yield of the fission in tetracene and the energy transfer to silicon is around 133 per cent, establishing the potential of singlet exciton fission to increase the efficiencies of silicon solar cells and reduce the cost of the energy that they generate.

Figure 1a shows how the absorption of photons in silicon wastes excess energy, and Fig. 1b displays the mechanism by which singlet exciton fission instead produces two electron–hole pairs¹⁰. As shown in Fig. 1c, photoexcitation of the 2.40-eV singlet exciton of tetracene in the blue or green region of the visible spectrum generates two triplet excitons with an energy of 1.25 eV each, which matches the bandgap of silicon at 1.11 eV almost perfectly^{11,12}. Energy transfer from tetracene to inorganic lead sulfide semiconductor nanocrystals has previously been demonstrated at high efficiencies^{13,14}. There have also been reports of triplet dissociation at silicon–tetracene heterojunctions¹⁵. However, experiments on hydrogen-passivated silicon with lithium fluoride interlayers have yielded no evidence of triplet transfer from tetracene to silicon^{16,17}. One reason might be the lack of a suitable bifunctional interlayer, which should allow transfer of charge carriers or excitons and provide sufficient passivation to prevent rapid recombination of charge carriers at the silicon surface^{18,19}. Passivation can be achieved through two methods: chemical passivation involves the reduction of recombination centres by saturating silicon dangling bonds, and field-effect passivation results from the repulsion of charge carriers, especially minority carriers, in response to an electric field present at the surface of the material. Most modern passivation layers rely on contributions from both approaches.

To permit tetracene charge carriers to tunnel into silicon, the silicon passivation interlayer should be a conformal dielectric grown with atomic control over its thickness, because the tunnelling probability decreases exponentially with the barrier width. We chose hafnium oxynitride (HfO_xN_y) for this purpose because it is insulating and can be grown on top of silicon wafers by atomic layer deposition²⁰. The atomic

concentrations of the elements for the interlayer were determined to be 57% hafnium, 22% nitrogen and 21% oxygen using X-ray photoelectron spectroscopy (see Supplementary Figs. 1–5). The bandgap was measured to be 4.28 eV using ultraviolet photoelectron spectroscopy and inverse photoemission spectroscopy; see Fig. 1d and Supplementary Figs. 6–9. Atomic force microscopy yielded a root-mean-square roughness of 150 pm (Extended Data Fig. 1). The overall structure is silicon– HfO_xN_y –tetracene, where the tetracene was thermally evaporated. The optimal thickness of HfO_xN_y was determined to be 8 Å, as discussed below. The tetracene thickness was kept constant at 30 nm.

Following a previously reported protocol²¹ we fabricate dopant-free interdigitated back-contacted silicon solar cells with aluminium/molybdenum oxide contacts for hole extraction and aluminium/lithium fluoride contacts for electron extraction. The solar cell device structure is shown in Fig. 2a and photographs of the devices are shown in Fig. 2b. See Methods and Extended Data Fig. 2 for further fabrication details. We subsequently protect the back contacts with a combination of polydimethylsiloxane (PDMS) and an additional piece of silicon, and perform a mild version of a Radio Corporation of America clean on the front surface of the silicon. We then fabricate the HfO_xN_y interlayer and tetracene film as described in Methods. We compare cells with 8-Å-thick HfO_xN_y interlayers to cells with 16-Å-thick HfO_xN_y interlayers. In these two devices, the optical properties are almost identical, but the thicker interlayer is expected to hinder charge and exciton tunnelling between tetracene and silicon, allowing us to isolate effects that stem from coupling at the interface. For characterization, we also fabricate samples without electrical back contacts that are otherwise identical to the samples described above. We henceforth refer to these samples as ‘photoluminescent’ after the detection methods used to characterize them.

The current–voltage characteristics of the solar cell devices with back contacts under AM1.5G solar spectrum illumination conditions are shown in Fig. 2c. The cell with the 16-Å-thick interlayer exhibits a short-circuit current of $I_{SC} = 4.6 \text{ mA cm}^{-2}$, an open-circuit voltage of $V_{OC} = 0.40 \text{ V}$, a fill factor of 48% and a power conversion efficiency of 0.9%. By contrast, the cell with the 8-Å-thick interlayer has $I_{SC} = 21.7 \text{ mA cm}^{-2}$, $V_{OC} = 0.46 \text{ V}$, a fill factor of 51% and a power conversion efficiency of 5.1%. This constitutes an almost fivefold increase in I_{SC} and an almost sixfold increase in power conversion efficiency, owing to the superior external quantum efficiency (EQE) of the 8-Å-thick HfO_xN_y device (Fig. 2d). Specifically, under a white-light bias, the EQE for the 8-Å-thick HfO_xN_y cell is higher than that of the 16-Å-thick HfO_xN_y cell by a factor of 6.6, at wavelengths longer than $\lambda = 560 \text{ nm}$. The cell with the thinner interlayer performs even better in the blue part of the spectrum, with a peak at $\lambda = 517 \text{ nm}$ (close to the tetracene absorption maximum at $\lambda = 524 \text{ nm}$), which represents an EQE 11.6 times greater than that of the 16-Å-thick interlayer cell. In fact, the shape of the relative improvement roughly matches the absorption of tetracene, but with notable broadening at longer wavelengths. The shape is analysed further below and compared to

¹Center for Excitonics, Massachusetts Institute of Technology (MIT), Cambridge, MA, USA. ²Department of Electrical Engineering, Princeton University, Princeton, NJ, USA. ³Department of Mechanical Engineering, Massachusetts Institute of Technology, Cambridge, MA, USA. ⁴Present address: The Rowland Institute at Harvard, Harvard University, Cambridge, MA, USA. ⁵These authors contributed equally: Markus Einzinger, Tony Wu. *e-mail: baldo@mit.edu

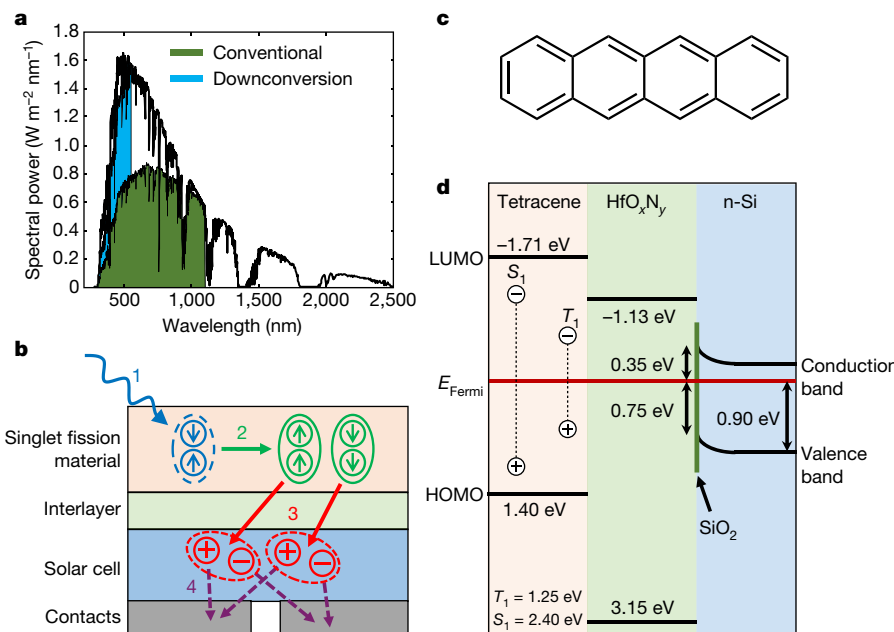


Fig. 1 | The concept of downconversion and the materials employed in this study. **a**, The solar spectrum. The green area indicates the power density that can be harvested in conventional silicon solar cells and the blue area indicates the possible gains from employing singlet-fission materials as downconverters. **b**, The downconversion process. 1, Light absorption; 2, singlet fission; 3, energy transfer; 4, hole and electron extraction. **c**, The molecular structure of tetracene. **d**, The

energetic structure of the system, as determined from ultraviolet photon spectroscopy (Supplementary Figs. 6–9). The vertical green line at the silicon surface indicates the location of a possible monolayer oxide coating formed immediately after surface cleaning. S_1 , singlet exciton energy; T_1 , triplet exciton energy; E_{Fermi} , Fermi energy of the system; LUMO, lowest unoccupied molecular orbital; HOMO, highest occupied molecular orbital; n-Si, phosphorus-doped silicon.

the photoluminescence excitation spectrum. The full spectral response including wavelengths greater than 640 nm is shown in Extended Data Fig. 3.

As summarized in Fig. 3a, we consider two possible causes for the enhancement in solar cell performance observed for the device with thinner HfO_xN_y interlayer. First, exciton dissociation at the interface between tetracene and silicon could cause charging of the interface and

thus electric-field-effect passivation. We note that such charging could be initiated by photoexcitation of either the tetracene or the silicon. Second, singlet fission in tetracene and the subsequent triplet energy transfer could enhance the photocurrent in the silicon.

To probe potential electronic or excitonic interactions between silicon and tetracene, we characterize the photoluminescent samples that do not have back contacts. As shown in Fig. 3b, we excite the

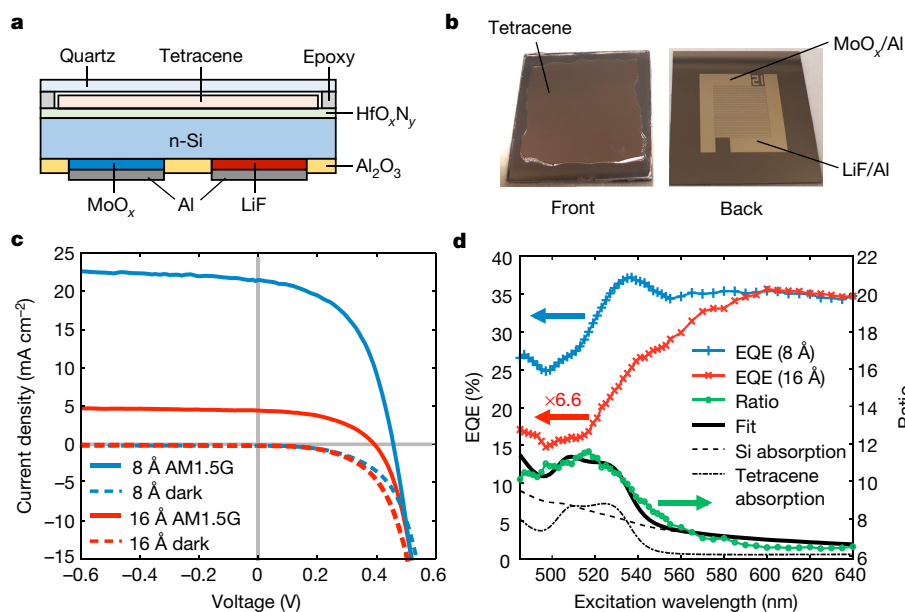


Fig. 2 | Photocurrent experiments. **a**, Device structure for a singlet-fission-sensitized silicon solar cell. **b**, Photograph of the solar cell with back contacts. **c**, Current–voltage characteristics for the solar cells with interlayer thicknesses of 8 Å (blue) and 16 Å (red). **d**, EQE spectra of solar cells with interlayer thicknesses of 8 Å and 16 Å. The EQE of the

16-Å-thick HfO_xN_y cell is scaled by 6.6 for comparison. The ratio of the EQE of the 8-Å-thick HfO_xN_y cell to that of the 16-Å-thick HfO_xN_y cell is shown in green and compared to a fit (black solid line) using the contributions of the silicon absorption (black dashed line) and tetracene absorption (black dash-dotted line).

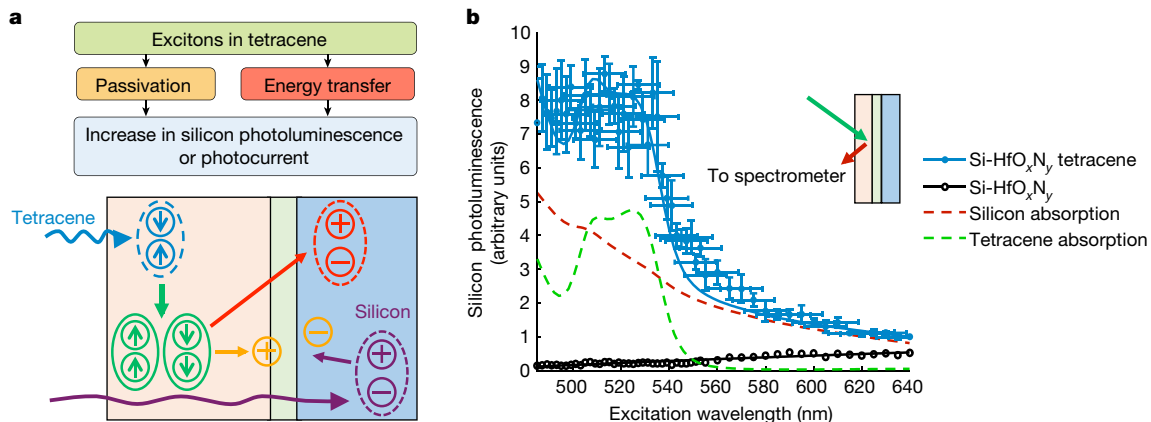


Fig. 3 | Photoluminescence experiments. **a**, Flow diagram summarizing the two pathways that increase silicon photoluminescence. Following photoexcitation of tetracene (blue) or silicon (dark purple), electric-field-effect passivation (orange charges) is caused by exciton dissociation at the interface or charge diffusion from the silicon. Additional electron-hole pairs in silicon can also be created by singlet exciton fission in tetracene (green) and triplet energy transfer (light red). **b**, Excitation

photoluminescent samples with and without tetracene (silicon-8-Å HfO_xN_y and silicon-8-Å HfO_xN_y-tetracene, respectively) using a variable-wavelength excitation source. We record their photoluminescence spectrum in the near infrared ($\lambda = 837\text{--}1,642\text{ nm}$), and additionally verify in Extended Data Fig. 4 that all of the photoluminescent samples show only emission from the silicon band-to-band transition, peaking at $\lambda = 1,144\text{ nm}$. The excitation spectra are shown in Fig. 3b. In this figure, the silicon photoluminescence of the photoluminescent sample without tetracene (black line with circles) increases with increasing wavelength. This trend is characteristic of surface recombination losses in silicon and is explained by the decreasing absorption coefficient of silicon at longer wavelengths (red dashed line in Fig. 3b). Charge carriers generated by longer-wavelength light are created deeper in the bulk of the wafer and have more time to radiatively recombine before they reach the interface.

We notice a stark difference when examining the excitation spectrum of the sample with the tetracene layer. The photoluminescence of the silicon in the sample is stronger at all wavelengths, increasing about eight times in the tetracene absorption region $\lambda < 550\text{ nm}$ compared

spectrum showing the beneficial influence of the tetracene coating on a photoluminescent silicon sample. The contributions of the silicon absorption (red dashed line) and the tetracene absorption (green dashed line) are shown. Vertical error bars are 1σ ; horizontal error bars are the spectral width of the excitation source at an intensity of e^{-2} ; $n = 1,600$. Inset, schematic of the measurement method.

to $\lambda = 640\text{ nm}$. Because fission and energy transfer are capable of at most a twofold enhancement, the data suggest an improvement in surface passivation during the illumination of tetracene. The behaviour is reversible when the wavelength is swept back and forth (Extended Data Fig. 5), and so we cannot attribute the effect to chemical passivation, for which we would expect a permanent modification. We instead explain this behaviour as an electric-field-effect passivation following generation of charge at the interface between the tetracene and the silicon. The excitation spectrum for $\lambda < 560\text{ nm}$ is proportional to the absorption spectrum of tetracene, and the tetracene absorption edge is clearly visible in Fig. 3b (blue solid line with circles and error bars). Similarly, the excitation spectrum for $\lambda > 560\text{ nm}$, where tetracene absorption is minimal, appears to be proportional to the absorption coefficient of silicon. We attribute this to the fact that more charge carriers are generated closer to the interface at higher absorption coefficients.

To further investigate the passivation properties of the silicon-HfO_xN_y-tetracene cell, we perform quasi-steady-state photoconductance decay measurements²². For an intrinsic silicon wafer passivated by 8-Å-thick layers of HfO_xN_y on both sides, the surface recombination

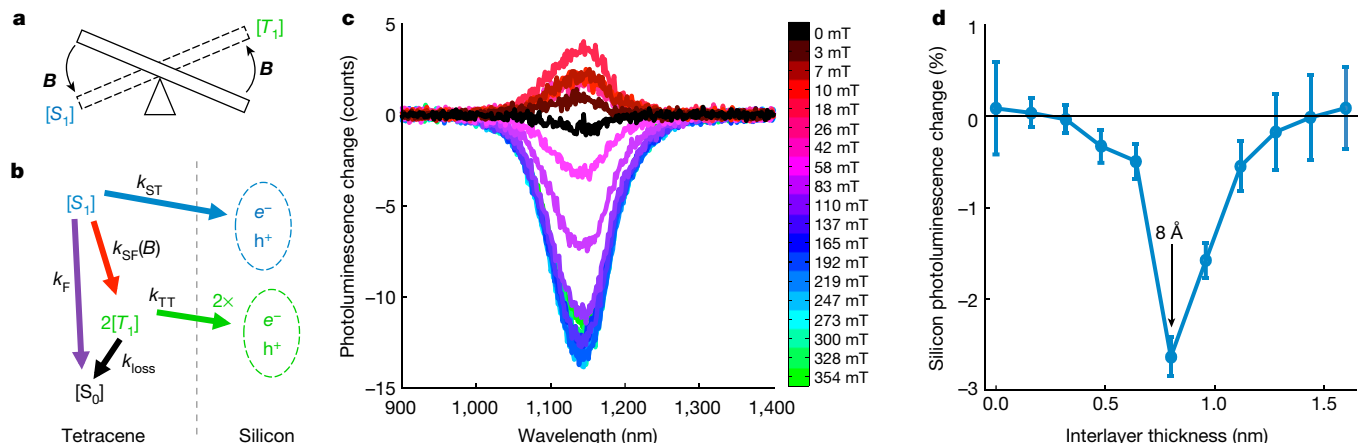


Fig. 4 | Effect of an applied magnetic field on the photoluminescence of silicon. **a**, Simplistic model of the effect of an applied magnetic field on singlet exciton fission. Application of a strong field ($B > 0.05\text{ T}$) increases the singlet exciton density, $[S_1]$, and decreases the triplet exciton density, $[T_1]$. **b**, Key processes at the tetracene–silicon interface. k_{ST} and k_{TT} are the rate constants of singlet and triplet exciton transfer, respectively; k_F is the tetracene fluorescence rate constant; k_{loss} is the rate constant of non-radiative triplet deactivation and $k_{SF}(B)$ is the net rate constant of

singlet exciton fission, which depends on the applied magnetic field B . e^- , electrons; h^+ , holes. **c**, The effect of a magnetic field on a silicon-8-Å-thick HfO_xN_y-tetracene photoluminescent sample excited at $\lambda = 532\text{ nm}$, measured as the change in photoluminescence for detection wavelengths between 900 and 1,400 nm. **d**, The effect of the applied magnetic field on photoluminescence depends on the thickness of the HfO_xN_y, with a clear peak at 8 Å. Error bars are 1σ ; $n = 4,000$.

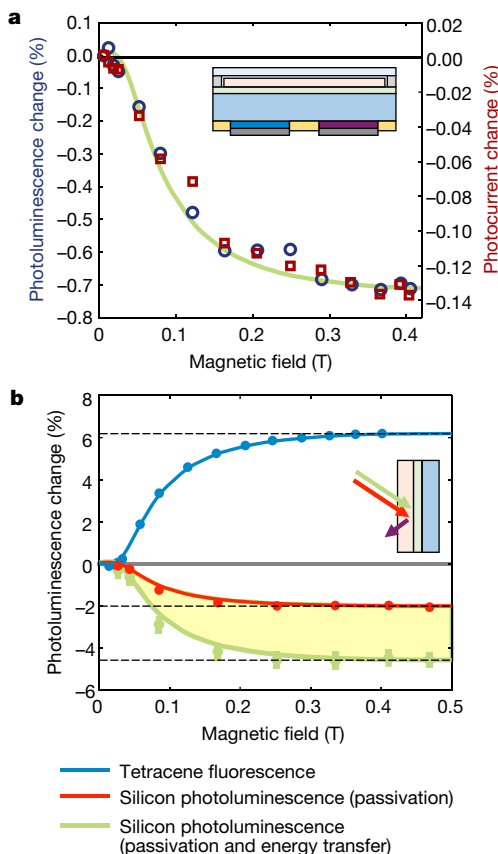


Fig. 5 | Exciton transfer yield. **a**, Effect of an applied magnetic field on sensitized solar cells. The negative trend demonstrates that singlet exciton fission in tetracene increases the efficiency of the solar cell. The effect on the photocurrent, however, is five times weaker than that on the photoluminescence. Inset, schematic of the solar cell, as in Fig. 2a. **b**, The effect of the applied magnetic field on the photoluminescence of photoluminescent samples photoexcited at $\lambda = 532$ nm. To quantify the electric-field-effect passivation we employ a second beam at $\lambda = 785$ nm that is sensitive to passivation changes but does not drive energy transfer from the tetracene. The solid lines in **a** and **b** are fits to the singlet fission characteristic in tetracene, as determined from the fluorescence. Error bars are 1σ ; $n = 4,000$ (silicon); $n = 216$ (tetracene). Inset, schematic of the bichromatic experiment with red and green lasers (see Methods section ‘Bichromatic experiment’).

velocity is $971 \pm 40 \text{ cm s}^{-1}$ with an effective lifetime of $15 \pm 1 \mu\text{s}$. With tetracene on the front surface, the effective lifetime increases to $27 \pm 1 \mu\text{s}$, corresponding to a velocity of $534 \pm 39 \text{ cm s}^{-1}$. After illumination with light of $\lambda = 460 \text{ nm}$ at 20 mW cm^{-2} for 60 s, the surface recombination velocity decreases to $173 \pm 34 \text{ cm s}^{-1}$ with an effective lifetime of $55 \pm 2 \mu\text{s}$, where the uncertainties are 1σ . We conclude that charge generation at the silicon–HfO_xN_y–tetracene interface shown in Fig. 3 causes electric-field-effect passivation and that it can be initiated by optically pumping tetracene or silicon. The same phenomena are observed in the solar cell excitation spectra in Fig. 2c. The ratio of the photocurrent in the 8-Å-thick and 16-Å-thick HfO_xN_y cells has equal contributions from tetracene and silicon, identical to the enhancement of photoluminescence seen in Fig. 3b, which confirms that the photoluminescence excitation spectrum represents the same interfacial processes as the device.

We perform magnetic-field-dependent spectroscopy to probe for the possible presence of triplet energy transfer in addition to the electric-field-effect passivation. The net singlet fission rate is the combination of forward and backward processes; the backward process can be manipulated by applying an external magnetic field^{23–25}.

For small magnetic fields, the overall singlet fission rate first increases, then decreases and plateaus, yielding a characteristic

dependence on the applied magnetic field. In Fig. 4a we show a simplistic model in which the presence of a strong magnetic field B shifts the balance in tetracene from triplets back to singlets, with a corresponding impact on the various processes that are shown in Fig. 4b. Experimentally, we place the sample between the poles of an electromagnet and excite it monochromatically at $\lambda = 532 \text{ nm}$. We show the silicon spectra in response to an external magnetic field in Fig. 4c, presented as a percentage change in the photoluminescence. We find that the silicon photoluminescence can be modulated by external magnetic fields, and our results agree well with the expected magnetic field dependence. At higher magnetic fields, we observe a corresponding decrease in silicon photoluminescence, demonstrating that triplet excitons are the dominant cause of the passivation effect on the silicon photoluminescent samples.

As shown in Fig. 4d, we measure the magnetic field dependence of the photoluminescence of silicon for several HfO_xN_y interlayer thicknesses between 0 nm and 1.6 nm at a resolution of 0.16 nm, where every data point corresponds to one additional atomic layer deposition cycle. For interlayers thinner than 0.8 nm, the effect of the magnetic field on photoluminescence, measured as a percentage change, decreases towards zero with decreasing interlayer thickness. We attribute this magnetic-field effect to a lack of chemical passivation. For interlayers thicker than 0.8 nm, the effect of the magnetic field on photoluminescence again decreases to zero. The fact that it is possible to turn this effect off by increasing the interlayer thickness suggests the presence of a tunnelling process.

We also determine the effect of the applied magnetic field on the photoluminescence and photocurrent I_{SC} of the 8-Å-thick HfO_xN_y cell. We find that triplet excitons positively contribute to both the photoluminescence in the solar cell and to the photocurrent (Fig. 5a), but we note that the effect on the cell’s photoluminescence is approximately five times stronger than the effect on the photocurrent through the cell. The photoluminescence and the photocurrent are probably generated at the front and back sides of the cell, respectively. Therefore, this difference indicates the losses in carrier collection from the front side. When we compare both measurements to those in the silicon–HfO_xN_y–tetracene structures that were not subjected to additional solar cell processing to create back contacts, we find that their photoluminescence modulation under a magnetic field is about seven times greater than that in the solar cells. Thus, our photoluminescent samples exhibit photoluminescence modulations about 35 times stronger than the photocurrent modulations in the solar cells. We conclude that the photoluminescent samples provide an excellent system in which to study triplet-state energy transfer.

To quantify the contributions of electric-field-effect passivation and possible exciton transfer in the photoluminescent samples, we perform bichromatic experiments in which we introduce a second probe beam at $\lambda = 785 \text{ nm}$ with a photon flux that is almost 18 times greater than that of the excitation beam at $\lambda = 532 \text{ nm}$. Because tetracene does not absorb light at 785 nm, this pump creates additional electron–hole pairs in silicon that are sensitive to electric-field-effect passivation but are not affected by the magnetic field, because they do not originate from tetracene. Therefore, this experiment is sensitive to effects resulting almost solely from passivation, whereas the monochromatic excitation experiment at $\lambda = 532 \text{ nm}$ also measures energy transfer. The behaviour can be reproduced using a variety of pump intensities across two orders of magnitude and also if the second probe beam is set at $\lambda = 632.8 \text{ nm}$ (Extended Data Figs. 6–9).

Using the data from the monochromatic and bichromatic photoluminescence measurements that are shown in Fig. 5b, we employ a model to quantify the exciton yields, defined as the number of excitons fully transferred into silicon divided by the number of singlet excitons created in tetracene (detailed in Supplementary Information sections C, D and Supplementary Figs. 10–16). By comparing the effects of the applied magnetic field on the photoluminescence of the samples, we obtain a peak total exciton yield of $133\% \pm 13\%$, which is composed of a singlet transfer yield of $56\% \pm 6\%$ and a triplet transfer yield of

76% ± 7%, demonstrating efficient triplet exciton transfer from tetracene to silicon.

As discussed in Supplementary Information, the dominant loss in the photoluminescent samples is from singlet transfer to silicon that bypasses exciton fission. Future work could employ exothermic singlet fission molecules with higher fission rates than tetracene. Additional spectroscopy studies will be required to identify and characterize the other dynamics, including the passivation and energy-transfer mechanisms. For example, triplet energy transfer may proceed via a Dexter process²⁶ with simultaneous transfer of electrons and holes, or it may be mediated by exciton dissociation. The energy level alignment at the silicon–HfO_xN_y–tetracene interface depicted in Fig. 1d suggests that triplet exciton dissociation is not energetically favoured; we suggest therefore that electric-field-effect passivation must be mediated by traps.

Looking towards the prospect of silicon solar cells operating beyond the single-junction limit, we note that the technological challenge is to achieve control over the thickness, stoichiometry and trap density of the passivation layer and the uppermost few atomic layers of the cell. The strong passivation effect observed in thin HfO_xN_y layers is a crucial advance because it alleviates the quenching of injected electron–hole pairs in silicon and also permits coupling between silicon and the triplet excited states in tetracene. The next step is to improve the efficiency of sensitized cells, which is at present limited by poor carrier collection from the front surface of the silicon. Thinner silicon and tighter control over materials, processing and fabrication will increase efficiency, with a corresponding improvement in the ratio between the effects of the magnetic field on the photoluminescence and the photocurrent of the cell.

Online content

Any methods, additional references, Nature Research reporting summaries, source data, extended data, supplementary information, acknowledgements, peer review information; details of author contributions and competing interests; and statements of data and code availability are available at <https://doi.org/10.1038/s41586-019-1339-4>.

Received: 13 July 2018; Accepted: 7 May 2019;

Published online 3 July 2019.

- Green, A. M. Commercial progress and challenges for photovoltaics. *Nat. Energy* **1**, 15015 (2016).
- Shockley, W. & Queisser, H. J. Detailed balance limit of efficiency of p–n junction solar cells. *J. Appl. Phys.* **32**, 510–519 (1961).
- Smith, M. B. & Michl, J. Singlet fission. *Chem. Rev.* **110**, 6891–6936 (2010).
- Smith, M. B. & Michl, J. Recent advances in singlet fission. *Annu. Rev. Phys. Chem.* **64**, 361–386 (2013).

- Yost, S. R. et al. A transferable model for singlet-fission kinetics. *Nat. Chem.* **6**, 492–497 (2014); corrigendum **6**, 649 (2014).
- Dexter, D. L. Two ideas on energy transfer phenomena: ion-pair effects involving the OH stretching mode, and sensitization of photovoltaic cells. *J. Lumin.* **18**–**19**, 779–784 (1979).
- Congreve, D. N. et al. External quantum efficiency above 100% in a singlet-exciton-fission-based organic photovoltaic cell. *Science* **340**, 334–337 (2013).
- Wu, T. C. et al. Singlet fission efficiency in tetracene-based organic solar cells. *Appl. Phys. Lett.* **104**, 193901 (2014).
- Rao, A. & Friend, R. H. Harnessing singlet exciton fission to break the Shockley–Queisser limit. *Nat. Rev. Mater.* **2**, 17063 (2017).
- Hanna, M. C. & Nozik, A. J. Solar conversion efficiency of photovoltaic and photoelectrolysis cells with carrier multiplication absorbers. *J. Appl. Phys.* **100**, 074510 (2006).
- Swenberg, C. E. & Stacy, W. T. Bimolecular radiationless transitions in crystalline tetracene. *Chem. Phys. Lett.* **2**, 327–328 (1968).
- Burdett, J. J., Gosztola, D. & Bardeen, C. J. The dependence of singlet exciton relaxation on excitation density and temperature in polycrystalline tetracene thin films: kinetic evidence for a dark intermediate state and implications for singlet fission. *J. Chem. Phys.* **135**, 214508 (2011).
- Tabachnyk, M. et al. Resonant energy transfer of triplet excitons from pentacene to PbSe nanocrystals. *Nat. Mater.* **13**, 1033–1038 (2014).
- Thompson, N. J. et al. Energy harvesting of non-emissive triplet excitons in tetracene by emissive PbS nanocrystals. *Nat. Mater.* **13**, 1039–1043 (2014).
- MacQueen, R. W. et al. Crystalline silicon solar cells with tetracene interlayers: the path to silicon-singlet fission heterojunction devices. *Mater. Horiz.* **5**, 1065–1075 (2018).
- Hayashi, T., Castner, T. G. & Boyd, R. W. Quenching of molecular fluorescence near the surface of a semiconductor. *Chem. Phys. Lett.* **94**, 461–466 (1983).
- Piland, G. B. et al. Dynamics of molecular excitons near a semiconductor surface studied by fluorescence quenching of polycrystalline tetracene on silicon. *Chem. Phys. Lett.* **601**, 33–38 (2014).
- Bonilla, R. S., Hoex, B., Hamer, P. & Wilshaw, P. R. Dielectric surface passivation for silicon solar cells: a review. *Phys. Status Solidi A* **214**, 1700293 (2017).
- Aberle, A. G. Surface passivation of crystalline silicon solar cells: a review. *Prog. Photovolt. Res. Appl.* **8**, 473–487 (2000).
- Becker, J. S., Kim, E. & Gordon, R. G. Atomic layer deposition of insulating hafnium and zirconium nitrides. *Chem. Mater.* **16**, 3497–3501 (2004).
- Um, H.-D. et al. Dopant-free all-back-contact Si nanohole solar cells using MoO_x and LiF films. *Nano Lett.* **16**, 981–987 (2016).
- Sinton, R. A. & Cuevas, A. Contactless determination of current–voltage characteristics and minority-carrier lifetimes in semiconductors from quasi-steady-state photoconductance data. *Appl. Phys. Lett.* **69**, 2510–2512 (1996).
- Geacintov, N., Pope, M. & Vogel, F. Effect of magnetic field on the fluorescence of tetracene crystals: exciton fission. *Phys. Rev. Lett.* **22**, 593–596 (1969).
- Merrifield, R. E., Avakian, P. & Groff, R. P. Fission of singlet excitons into pairs of triplet excitons in tetracene crystals. *Chem. Phys. Lett.* **3**, 386–388 (1969).
- Suna, A. Kinematics of exciton–exciton annihilation in molecular crystals. *Phys. Rev. B* **1**, 1716–1739 (1970).
- Dexter, D. L. A theory of sensitized luminescence in solids. *J. Chem. Phys.* **21**, 836–850 (1953).

Publisher's note: Springer Nature remains neutral with regard to jurisdictional claims in published maps and institutional affiliations.

© The Author(s), under exclusive licence to Springer Nature Limited 2019

METHODS

Device fabrication. For a schematic of the fabrication process, see Extended Data Fig. 2. We purchased silicon wafers from PureWafer (for details see Supplementary Table 3) and transferred them to a clean room. We then performed a standard Radio Corporation of America (RCA) clean as follows. First, organic contaminants were removed by immersing the sample in a 5:1:1 ratio solution of deionized water, aqueous ammonium hydroxide (29%), and aqueous hydrogen peroxide (30%) for 20 min at 80 °C. Second, the native oxide was removed by etching with aqueous hydrofluoric acid (1%) for 60 s. Third, metal-ion contaminants were removed from the wafer surface in a 5:1:1 ratio solution of deionized water, aqueous hydrochloric acid (37%), and aqueous hydrogen peroxide (30%) for 20 min at 80 °C. We then deposited 10 nm of aluminium oxide on both sides using atomic layer deposition. Using photolithography, we fabricated electron-selective contacts (aluminium/lithium fluoride) and hole-selective contacts (aluminium/molybdenum oxide) in an interdigitated fashion. We then diced the wafers into chips and protected the back side of the individual chips using PDMS and a second piece of encapsulating silicon to provide a seal. We experimentally verify in Extended Data Fig. 10 that a full RCA clean before HfO_xN_y deposition is not compatible with our solar cell fabrication because the protective rear PDMS seal decomposes in the presence of acids, and the monomers subsequently reattach to the front side by condensation^{27,28}. Consequently, to minimize contamination by PDMS in this process, we cleaned the front side using 10% aqueous hydrofluoric acid for 1 min and a 5:1:1 ratio solution of deionized water, aqueous ammonium hydroxide (29%) and aqueous hydrogen peroxide (30%) for 20 min at 60 °C. We fabricated the downconversion front side as detailed below and then peeled off the silicon protecting the back contacts (as shown in Extended Data Fig. 2).

Photoluminescent sample fabrication. The silicon wafers for the photoluminescent samples were purchased from EL-CAT (for details see Supplementary Table 3) and transferred to a clean room, and were then diced and cleaned using a standard RCA clean (see Methods section ‘Device fabrication’). We then fabricated the downconversion front side as detailed below.

Downconversion front-side fabrication. HfO_xN_y was deposited using atomic layer deposition in a Cambridge Nanotech Savannah deposition system²². We used tetrakis(dimethylamino)hafnium as the hafnium precursor and ammonia as the nitrogen precursor with residual oxygen in the chamber. The hafnium injection pulse duration was 30 ms and the ammonia injection pulse duration was 20 ms. The hafnium precursor was at an initial temperature of 95 °C, and the reaction chamber was heated to 150 °C during the growth of the HfO_xN_y. The base pressure at a nitrogen flow of 40 cm³ min⁻¹ was 0.4 torr. The samples were immediately transferred into a nitrogen glovebox. Finally, 30 nm of tetracene was deposited at a rate of 1 Å s⁻¹ by thermal evaporation in a vacuum chamber with base pressure <1 × 10⁻⁶ torr, directly connected to the glovebox. The tetracene used in this work was received from Sigma Aldrich (98% purity) and purified by sublimation in a tube furnace three consecutive times. Samples were packaged in a nitrogen glovebox using ultraviolet-curing epoxy and a quartz slide at oxygen and water concentrations below 5 p.p.m. The active area of the substrates was protected with aluminium foil during ultraviolet exposure.

Photoelectron spectroscopy. Ultraviolet photoelectron spectroscopy, X-ray photoelectron spectroscopy and inverse photoemission spectroscopy experiments were conducted in an ultrahigh-vacuum chamber with a base pressure of 5 × 10⁻¹⁰ torr. Ultraviolet photoelectron spectroscopy measurements were done with both the He I (21.22 eV) and He II (40.81 eV) photon lines generated by a discharge lamp. Non-monochromated aluminium K α X-rays with an energy of 1,486.6 eV were used for all X-ray photoelectron spectroscopy measurements. Inverse photoemission spectroscopy was performed in the isochromat mode with a setup described elsewhere²⁹. The nominal energy resolutions for ultraviolet photoelectron spectroscopy, X-ray photoelectron spectroscopy and inverse photoemission spectroscopy were 100 meV, 800 meV and 400 meV, respectively. A tetracene layer with a thickness of 4 nm was deposited on the HfO_xN_y–silicon surfaces in an ultrahigh-vacuum chamber connected to the analysis chamber by thermal evaporation at rates of about 1 Å s⁻¹.

Device experiments. Current–voltage characteristics were recorded using a precision semiconductor parameter analyser (Agilent 4156C) in voltage mode sweeping from −0.6 V to +0.6 V in 10 mV intervals. The sample was illuminated through a shadow mask using a calibrated solar simulator (Newport 69920) emitting an AM1.5G solar spectrum. The EQE data was collected using a broadband tunable laser (SuperK EXTREME supercontinuum) or a tungsten lamp with monochromator as the excitation source under a white-light bias.

Excitation spectrum. A broadband tunable laser (SuperK EXTREME supercontinuum laser) was focused onto the sample with 20-ps pulses at 78 MHz. The infrared emission from the sample was collected by a liquid-nitrogen-cooled InGaAs detector (Princeton Instruments OMA V). The excitation wavelength was varied from 485 nm to 640 nm, but the photon fluxes were kept constant,

corresponding to optical intensities of 458 mW cm⁻² to 344 mW cm⁻². This was achieved by adjusting the photon flux for every wavelength using a beam splitter, a photodetector and a software-based feedback loop. For a schematic of the setup see Supplementary Fig. 17.

Surface recombination velocity. Photoconductance decay measurements were performed using the silicon lifetime and wafer metrology system WCT-120 from Sinton Instruments (fully compliant with the industry standard SEMI PV-13)²². The optical constants were calculated taking into account the reflection and absorption of all layers on top of the silicon. Where applicable, the transfer matrix method was used. The measured effective lifetimes were then used to determine the surface recombination velocities (see Supplementary Information section F).

Monochromatic experiments. The samples were excited with a Coherent Genesis MX532-500 STM laser at 532 nm (8.2 mW cm⁻²). Infrared emission from the samples was collected with a liquid-nitrogen-cooled InGaAs detector (Princeton Instruments OMA V). A pulsed external magnetic field of varying strength was applied and the spectra were recorded continuously. The laser intensity was monitored using a 90:10 (transmission:reflection) beam splitter and a silicon photodetector (Newport 818-SL). For a schematic of the setup see Supplementary Fig. 18. In the experiment in which we performed photoluminescence and photocurrent measurements simultaneously, we excited the sample with a Coherent Verdi G laser at 532 nm (25 W cm⁻²) chopped at 313 Hz. The bias point was approximately 0.16 V. The silicon photoluminescence was measured with a germanium photodetector (Newport 818-IR) connected to a lock-in amplifier (SR830, Stanford Research Systems) and the photocurrent was measured as the current across a 50-Ω resistor, connected to a second lock-in amplifier (SR830, Stanford Research Systems).

Bichromatic experiment. The beams of two lasers (Coherent Genesis MX532-500 STM and Thorlabs LDM 785) at 532 nm and 785 nm were merged using a 90:10 beam splitter. The photon flux of the 785-nm beam was chosen to be almost 18 times stronger than that of the 532 nm pump. The optical intensities were 8.2 mW cm⁻² and 198 mW cm⁻² for the 532-nm and 785-nm beams, respectively. The tetracene emission was collected with a silicon photodetector (Newport 818-SL) connected to a lock-in amplifier (SR830, Stanford Research Systems). Otherwise, this measurement was identical to the monochromatic experiment described above. For a schematic of the setup see Supplementary Fig. 19.

Modelling. The model used to calculate the yield is described in Supplementary Information sections C, D and Supplementary Figs. 10–16. The model was implemented using a custom MATLAB code.

Data availability

The data that support the findings of this study are available from the corresponding author upon reasonable request.

Code availability

The custom code that supports the findings of this study is available from the corresponding author upon reasonable request.

- 27. Mata, A., Fleischman, A. J. & Roy, S. Characterization of polydimethylsiloxane (PDMS) properties for biomedical micro/nanosystems. *Biomed. Microdevices* **7**, 281–293 (2005).
- 28. Kim, Y.-K., Kim, G. T. & Ha, J. S. Simple patterning via adhesion between a buffered-oxide etchant-treated PDMS stamp and a SiO₂ substrate. *Adv. Funct. Mater.* **17**, 2125–2132 (2007).
- 29. Wu, C. I., Hirose, Y., Sirringhaus, H. & Kahn, A. Electron–hole interaction energy in the organic molecular semiconductor PTCDA. *Chem. Phys. Lett.* **272**, 43–47 (1997).

Acknowledgements This work was supported through the Center for Excitonics, an Energy Frontier Research Center, by the US Department of Energy, Office of Science, Office of Basic Energy Sciences under award number DE-SC0001088 (MIT). Surface characterization work at Princeton was supported in part by the U.S. Department of Energy, Office of Basic Energy Sciences, Division of Materials Sciences and Engineering under award DE-SC0012458 (A.K.) and the National Science Foundation Graduate Research Fellowship grant DGE-1656466 (H.L.S.). We thank T. Buonassisi for access to the silicon lifetime and wafer metrology system. We thank D.-G. Ha for help with the atomic force microscopy measurements.

Author contributions M.E. and T.W. fabricated the photoluminescent samples and measured the photoluminescent excitation spectra and the effect of the magnetic field on photoluminescence. M.E., T.W. and C.F.P. built the setup for the measurements of the effect of the magnetic field on photoluminescence. J.F.K. and M.E. fabricated the solar cells. M.E. and J.F.K. performed solar cell measurements (current–voltage and EQE measurements, and measurements of the effects of the magnetic field). M.E., L.N. and S.W. performed the photoconductance decay measurements. H.L.S. performed the ultraviolet photoelectron spectroscopy and inverse photoemission spectroscopy

measurements. H.L.S. and M.E. performed the X-ray photoelectron spectroscopy measurements. M.A.B., M.E., D.N.C. and T.W. conceived the project. A.K., M.G.B. and M.A.B. supervised the experiments. All authors discussed the results and commented on the manuscript.

Competing interests MIT has filed a provisional application for a US patent based on this technology that names M.E., T.W. and M.A.B. as inventors (serial number 62/678,818).

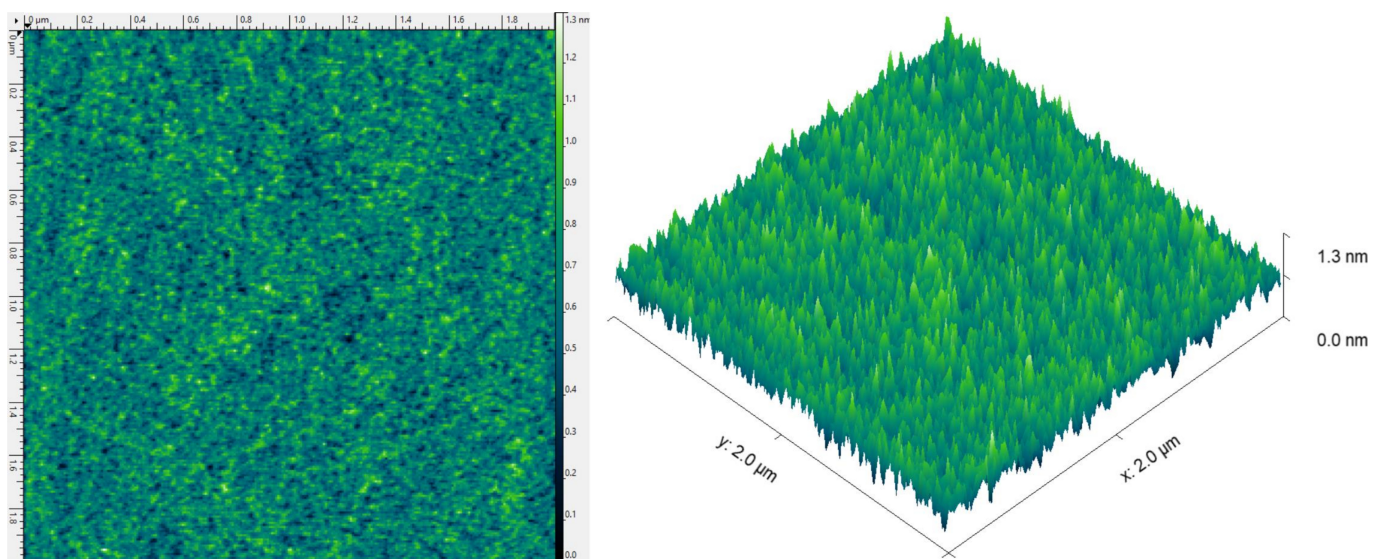
Additional information

Supplementary information is available for this paper at <https://doi.org/10.1038/s41586-019-1339-4>.

Correspondence and requests for materials should be addressed to M.A.B.

Peer review information *Nature* thanks Akshay Rao and the other anonymous reviewer(s) for their contribution to the peer review of this work.

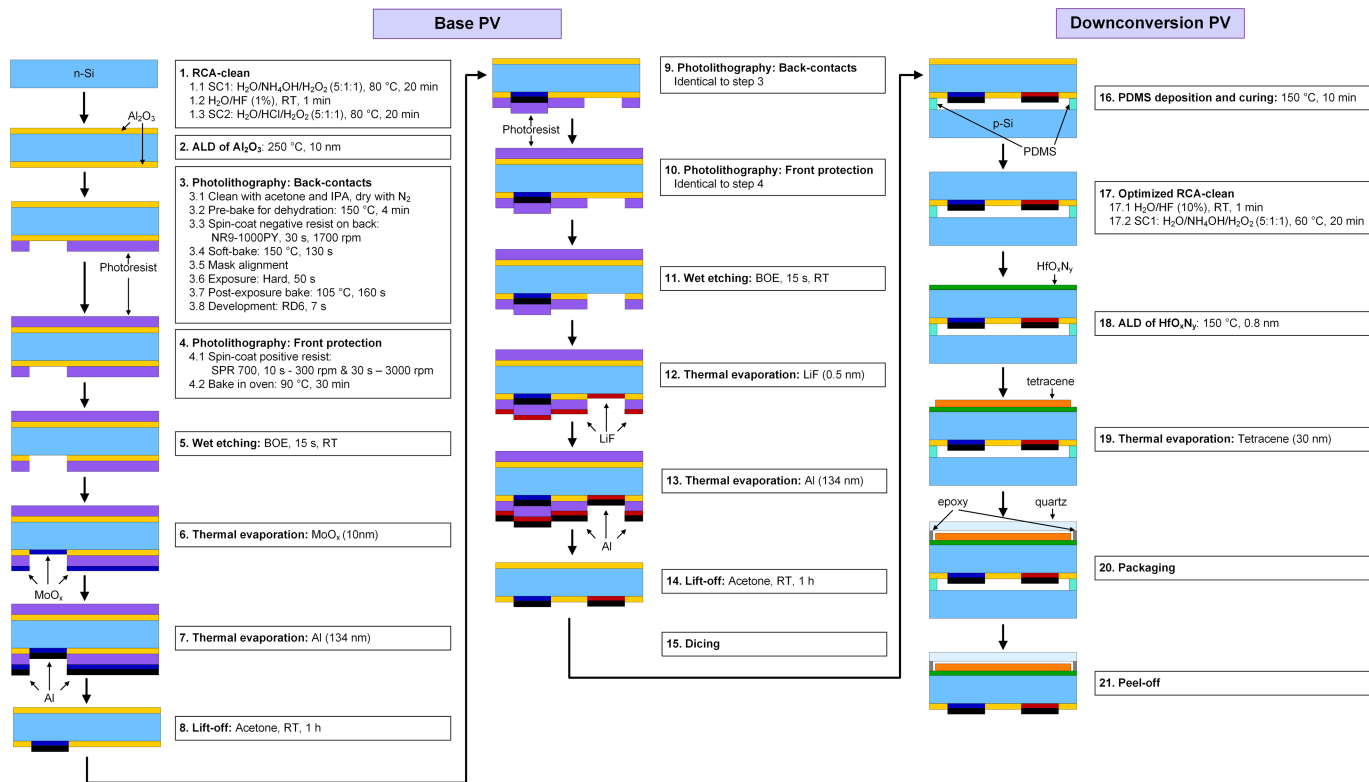
Reprints and permissions information is available at <http://www.nature.com/reprints>.



RMS roughness	150 pm
Mean roughness	120 pm
Excess kurtosis	0.00043

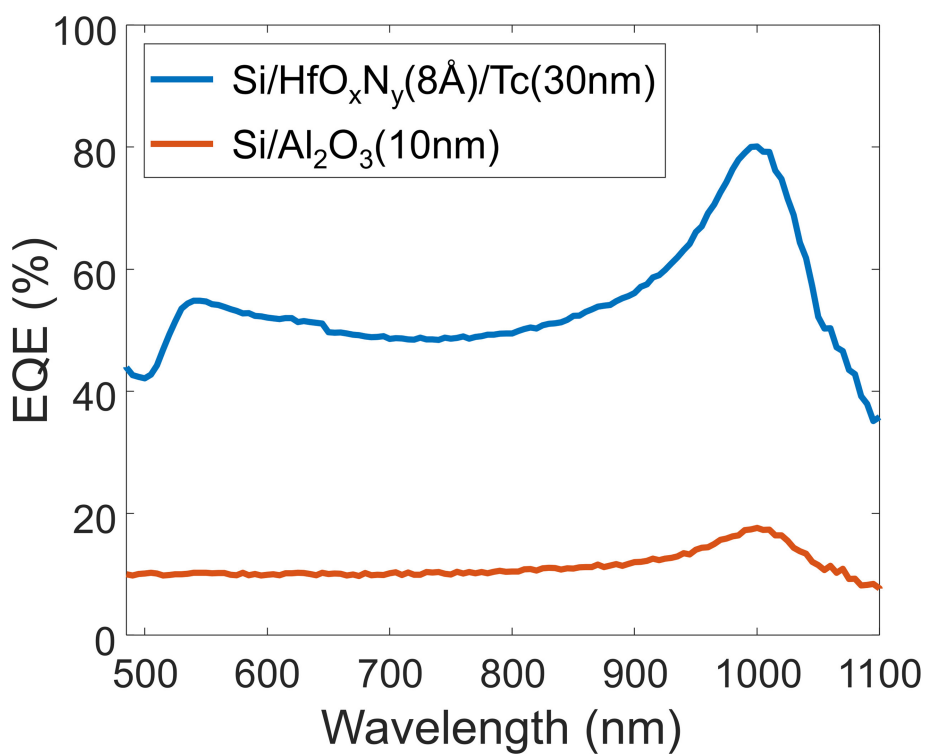
Extended Data Fig. 1 | Atomic force microscopy data of HfO_xN_y (8 Å, five atomic layer deposition cycles) on silicon. The film quality was monitored using atomic force microscopy (Veeco Metrology Nanoscope

V 3100 SPM; tip, HQ:NSC14/AL BS). The film thickness was monitored using ellipsometry (J. A. Woollam VASE ellipsometer). 500 cycles correspond to a thickness of 83 nm. RMS, root mean square.



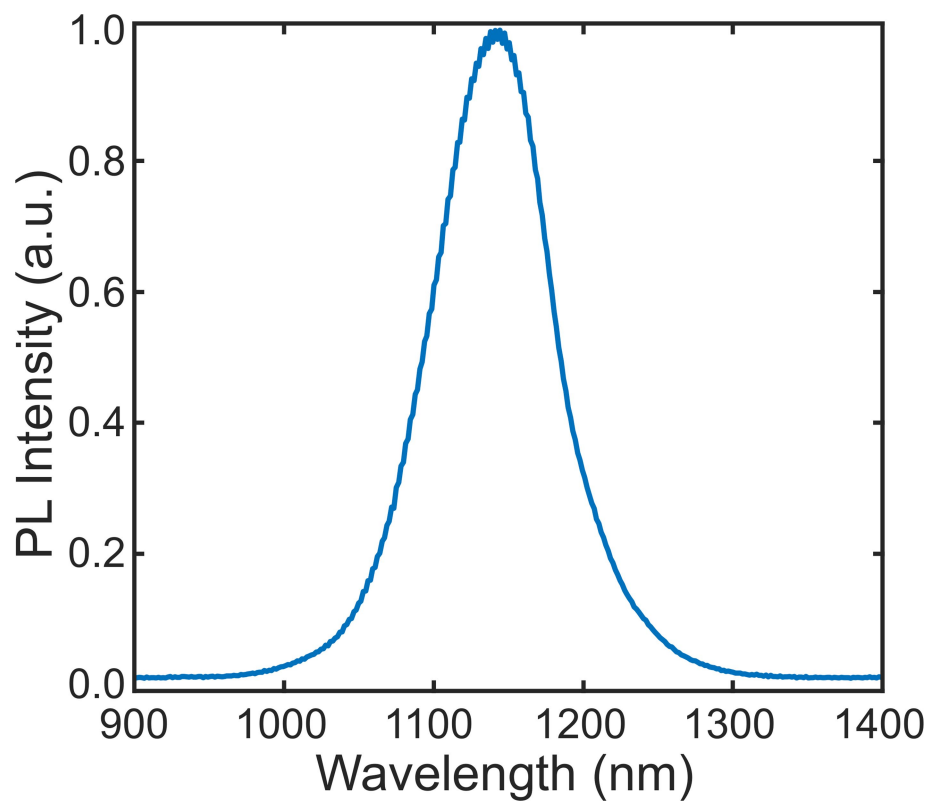
Extended Data Fig. 2 | Fabrication process of singlet-fission-enhanced silicon solar cells. Steps 1–14 are based on a previous work²¹. BOE, buffered oxide etch. RT, room temperature. ALD, atomic layer deposition; IPA, isopropylalcohol; NR9-1000PY; negative-tone photoresist designed

for 365 nm wavelength exposure; RD6, resist developer; SC1, RCA standard clean 1; SC2, RCA standard clean 2; PV, photovoltaic cell; p-Si, boron-doped silicon.

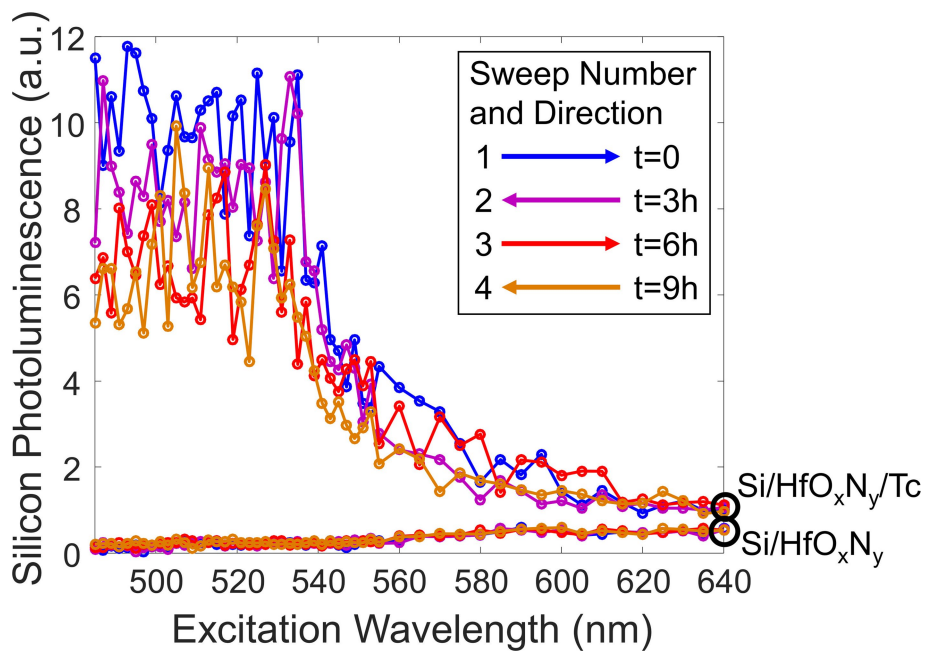


Extended Data Fig. 3 | Short-wavelength infrared EQE spectra for a tetracene-coated silicon solar cell (silicon-8-Å HfO_xN_y-30 nm tetracene) and a silicon solar cell without tetracene (silicon-10 nm aluminium oxide). Devices are fabricated using the procedures described in Methods and show increases in EQE at long wavelengths, potentially

due to poor carrier collection from the front of the cell. We note that in the absence of tetracene, there is ineffective thin-HfO_xN_y passivation. Silicon-8-Å-HfO_xN_y devices generate negligible photocurrent, in agreement with our measurements of the surface recombination velocity in the absence of tetracene. Tc, tetracene.

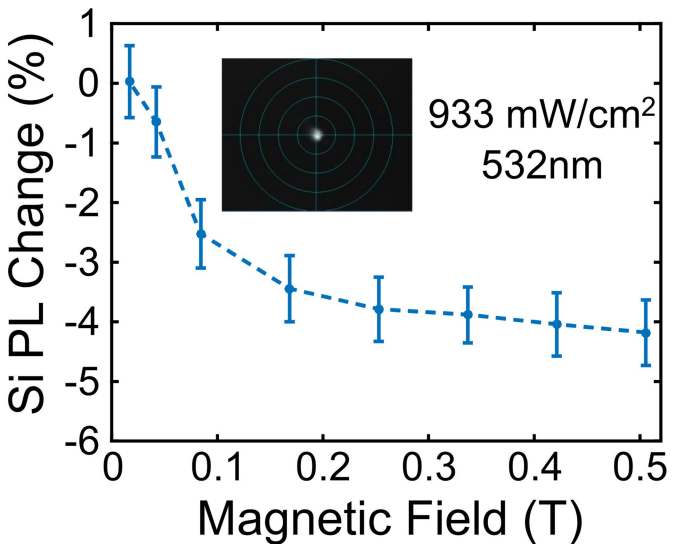
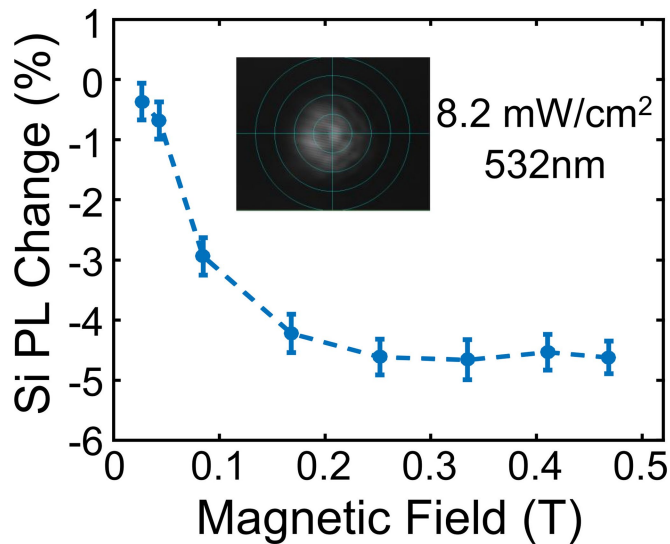


Extended Data Fig. 4 | Silicon photoluminescence (PL) spectrum corresponding to the band-to-band transition. The peak is at 1,144 nm (1.1 eV).



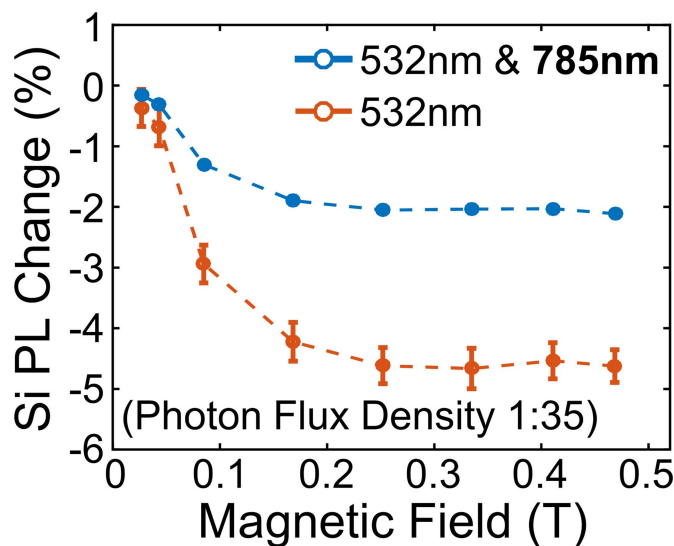
Extended Data Fig. 5 | Degradation for wavelength sweeps in the excitation spectrum. Arrows indicate the direction of the wavelength sweep (from short to long wavelengths or vice versa). The time t indicates

the start time of the sweep relative to the start of the entire measurement.
a.u., arbitrary units.

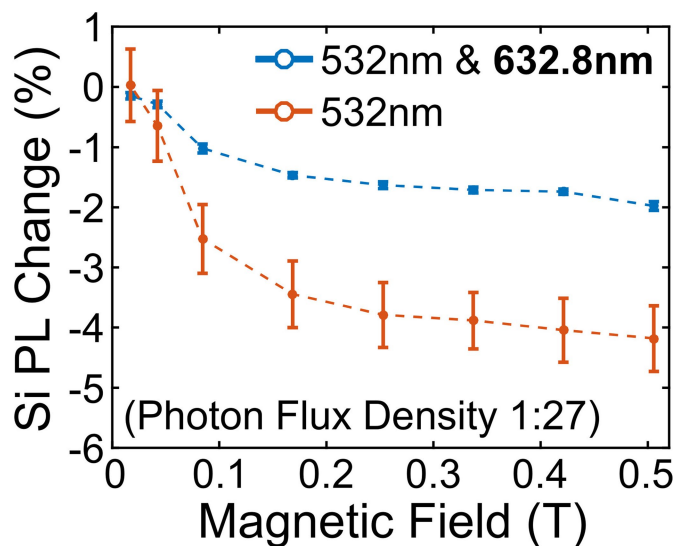


Extended Data Fig. 6 | Dependence of the change in photoluminescence from the applied magnetic field on the optical intensity (pump power density). Exciting the sample with vastly different intensities (left,

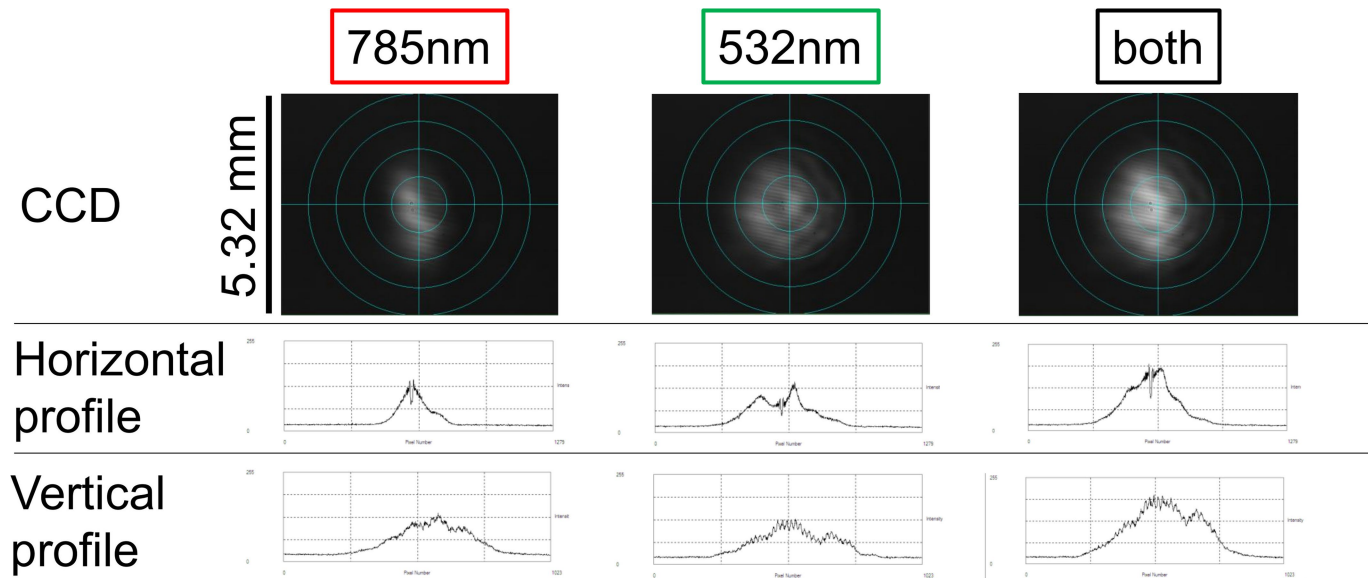
8.2 mW cm⁻² and right, 933 mW cm⁻²) yields a similar effect on the change in photoluminescence (-4.7% and -4.2%, respectively). Error bars are 1 σ ; n = 4,000.



Extended Data Fig. 7 | Bichromatic experiments with different probe beam wavelengths. The choice of the second pump wavelength (left, 785 nm; right, 632.8 nm) has no influence on the change in photoluminescence from the application of the magnetic field (about -2.0% for both secondary wavelengths). This excludes the possibility that any effects resulting from the choice of the second pump beam impair

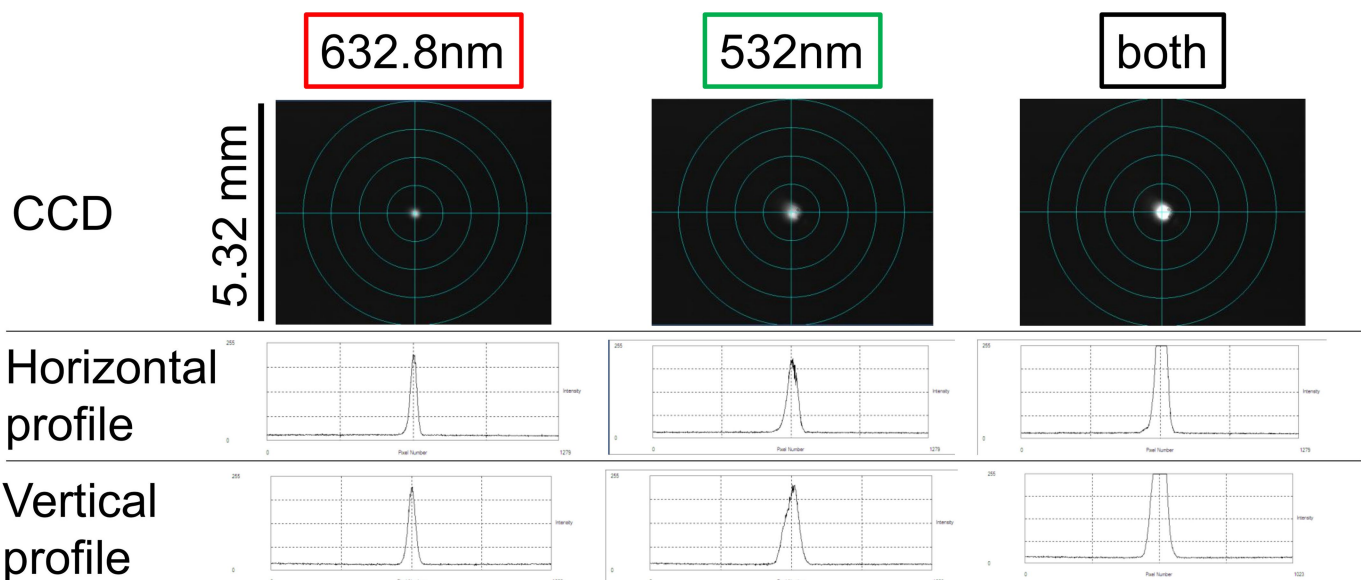


our determination of the exciton yield. The ratio of the flux density is calculated by comparing the number of incident photons per second from the two pump beams. The photon flux density of the 785 nm beam is 35 times larger than that of the 532 nm beam and the photon flux density of the 632.8 nm beam is 27 times larger than that of the 532 nm beam. Error bars are 1σ ; $n = 4,000$.



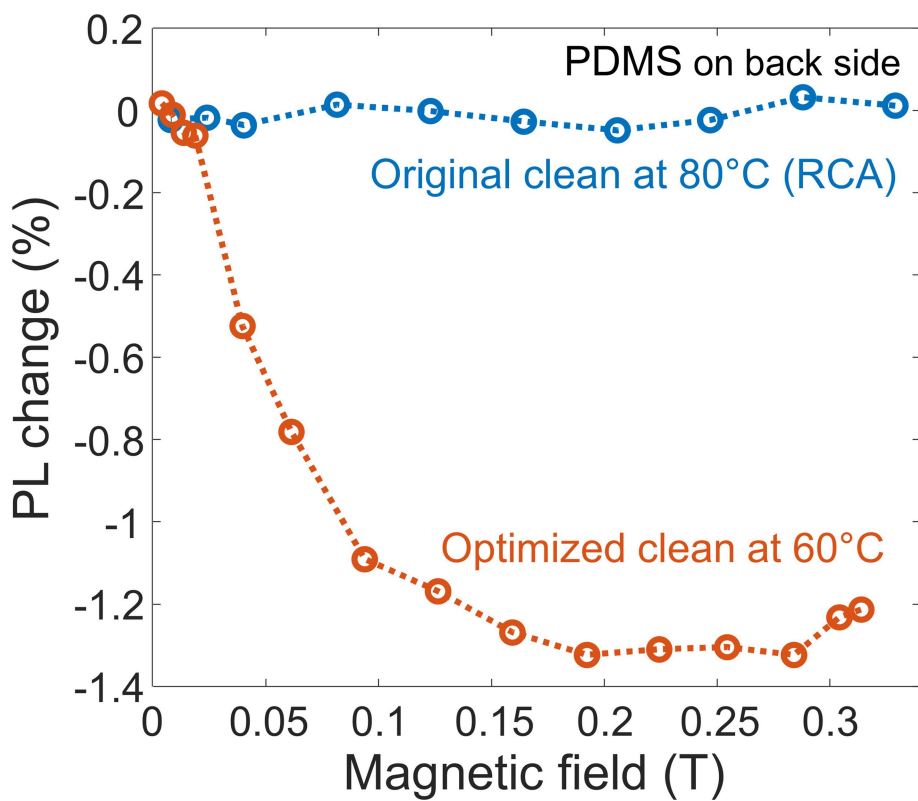
Extended Data Fig. 8 | Beam alignment for the bichromatic experiment
with the second probe at 632.8 nm. The green beam (Genesis, 532 nm)
influences the surface properties through passivation, and so must

cover the same area or a larger area than the red beam (Thorlabs HeNe,
632.8 nm). CCD, charge-coupled device.



Extended Data Fig. 9 | Beam alignment for the bichromatic experiment with the second probe at 785 nm. The green beam (Genesis, 532 nm) influences the surface properties through passivation, and so must

cover the same or a larger area than the red beam (Thorlabs photodiode, 785 nm).



Extended Data Fig. 10 | Back protection using PDMS. During device fabrication, we protect the back contacts using PDMS and an encapsulating piece of silicon to provide a seal during the front-side cleaning step. Here we show that the presence of PDMS on the back side can corrupt the integrity of the front surface. A full RCA clean of the front

surface at 80 °C shows no change in photoluminescence under an applied magnetic field. Using a milder version of the clean at 60 °C partly alleviates the issue but the change in photoluminescence from the applied magnetic field is not as large as in the samples processed without PDMS (see Fig. 5).